Research Square

Preprints are preliminary reports that have not undergone peer review.
They should not be considered conclusive, used to inform clinical practice,
or referenced by the media as validated information.

Bright and stable Cr3+-activated protoenstatite near-infrared emitter

Lei Zhou

zhoul8@mail.sysu.edu.cn

Sun Yat-sen University https://orcid.org/0000-0001-6942-5363

Lei Zhong

Sun Yat-sen University https://orcid.org/0000-0001-8806-2457

Yuefei Xiang

Sun Yat-sen University https://orcid.org/0000-0002-8966-2267

Zhe Wu

Sun Yat-sen University

Junfu Tang

Sun Yat-sen University

Shidan Rao

Sun Yat-sen University

Chunyan Jiang

South China Normal University

Xiao-Jun Wang

Georgia Southern University https://orcid.org/0000-0003-1506-0762

Mingmei Wu

Sun Yat-sen University https://orcid.org/0000-0001-8087-3925

Article

Keywords:

Posted Date: June 8th, 2026

DOI: https://doi.org/10.21203/rs.3.rs-9341929/v1

License: This work is licensed under a Creative Commons Attribution 4.0 International License.
Read Full License

Additional Declarations: There is **NO** Competing Interest.

Abstract

Broadband near-infrared (NIR) light sources that combine high power, high efficiency, and wide spectral coverage are essential for emerging applications in imaging, sensing, and illumination. Phosphor-converted light-emitting diodes (pc-LEDs) offer a scalable platform for such sources, but their performance is often limited by weak visible-light absorption of *d*-electron emitters originating from parity-forbidden transitions. Here we report a symmetry engineering strategy that overcomes this limitation by partially relaxing the parity selection rules in Cr^{3+}-activated systems. Controlled lattice perturbations in a rigid silicate framework break the local symmetry of Cr^{3+}-coordinating octahedra, significantly enhancing blue-light absorption without increasing dopant concentration. In parallel, crystallographically distinct sites enable efficient inter-site energy funneling, directing excitation toward energetically favourable emission centers and improving radiative efficiency. The optimized phosphor exhibits broadband NIR emission at λ_{max} ~ 880 nm with an internal and external quantum efficiency of 93% and 64%, among the highest reported values and along with excellent thermal and environmental stability. When integrated with a blue InGaN chip, the phosphor-converted device enables watt-level NIR output with excellent operational stability. These results highlight the role of local structural control in improving the performance of d-electron emitters and provide a viable route towards efficient broadband NIR light sources.

Introduction

Broadband near-infrared (NIR) light sources are increasingly important for diverse applications, including noninvasive sensing, night-vision surveillance, automotive safety and optical diagnostics[1, 2, 3, 4]. However, current NIR light-source technologies remain fundamentally limited. Tungsten–halogen lamps are inefficient and bulky, while semiconductor light-emitting diodes (LEDs) and lasers typically involve high fabrication costs, limited emission bandwidths, or complex thermal management requirements[5]. These limitations highlight the need for alternative photonic platforms that can deliver broadband, efficient, and scalable NIR emission. Phosphor-converted LEDs (pc-LEDs), which combine a commercial blue LED chip with down-converting NIR phosphors, offer a promising alternative for compact, reliable, and scalable NIR illumination[6]. Compared with coherent laser-driven systems, NIR pc-LEDs offer significant advantages such as suppressed speckle noise, low cost, and compatibility with wide-field imaging, making them prime candidates for next-generation NIR technologies.

Developing high-performance broadband NIR pc-LEDs critically depends on phosphors that can simultaneously exhibit efficient blue-light absorption, high external quantum efficiency (EQE), and robust thermal and environmental stability. Achieving broadband NIR luminescence with these comprehensive properties is one of the long-standing key challenges in photophysics. Among candidate emitters, trivalent chromium (Cr^{3+}) is a promising activator for broadband NIR emission due to its spin-allowed *d*–*d* transitions, which can generate wide emission bands spanning the first biological window[7]. The emission wavelength and bandwidth of Cr^{3+} are highly sensitive to the local crystal-field environment,

enabling tunability through host lattice selection and local structural modulation[8, 9]. However, these transitions are intrinsically limited by their parity-forbidden nature under centrosymmetric coordination, resulting in suboptimal absorption in the visible region. Consequently, efficient blue-light excitation often requires high dopant concentration, which triggers concentration quenching and increased non-radiative losses[10, 11]. This fundamental trade-off between absorption strength and quantum efficiency remains a central challenge in *d*-electron photophysics and limits the performance of NIR pc-LEDs.

One approach to address this limitation is to modify the local coordination environment of the activator. Specifically, reducing local site symmetry and augmenting octahedral distortion partially relaxes the Laporte-forbidden *d*–*d* transitions, thereby boosting the Cr^{3+} absorption cross-section without requiring high dopant concentrations[12, 13]. In parallel, structural features such as multiple crystallographic sites can introduce energy transfer pathways that redistribute excitation among luminescent centers. These effects are particularly effective in rigid host lattices, where non-radiative losses are suppressed and thermal stability is maintained[14]. Despite these advances, achieving a balanced combination of efficient excitation, high quantum yield and broadband emission in a chemically and thermally robust system remains challenging.

Magnesium silicates offer a versatile and low-cost structural platform for luminescent materials owing to their readily dopable Mg^{2+} sites and abundant elemental reserves[15, 16]. In particular, *Pbcn*-phase $MgSiO_3$ (protoenstatite) offers a rigid framework with multiple crystallographically distinct and strongly distorted Mg^{2+} sites[17, 18]. This enables tailored local crystal-field regulation, amplifying Cr^{3+} absorption and facilitating inter-site energy transfer. However, stabilizing the pure protoenstatite phase is challenging because it spontaneously transforms to the $P2_1/c$ phase[19]. Here, we demonstrate that co-doping Cr^{3+} and Li^+ enables synthesis of stable and single-phase protoenstatite (Supplementary Fig. 1). In this system, Li^+ incorporation induces controlled distortion of $[MgO_6]$ octahedra and modulates Cr^{3+} site distribution. This enhances optical absorption and optimizes radiative dynamics. The resulting $MgSiO_3$:Cr,Li phosphor exhibits bright, stable broadband NIR emission with high EQE and excellent thermal and chemical robustness. When integrated into pc-LEDs, this phosphor delivers watt-level NIR output with stable operation, highlighting the potential of local structural engineering in rigid silicate frameworks for high-power NIR optoelectronics.

Results and discussion

Protoenstatite crystallizes in an orthorhombic crystal system with the *Pbcn* space group (no. 60) and the chemical composition $MgSiO_3$, in which Mg and Si atoms are coordinated by six and four oxygen atoms, forming octahedral and tetrahedral sites, respectively (Fig. 1a) [20, 21]. The unit cell contains two crystallographically distinct Mg^{2+} sites occupying distorted octahedral sites with C_1 symmetry, both of which can be substituted by Cr^{3+} activators. Among them, the Mg1 site is more distorted than Mg2, leading to a pronounced breaking of inversion symmetry. Consequently, Cr^{3+} activators at Mg1 sites are

expected to exhibit significantly enhanced electric dipole transition probabilities. The relationship between local structure and optical properties will be discussed in detail below. The X-ray diffraction (XRD) patterns of $MgSiO_3$:*x*%Cr,Li phosphors synthesized *via* high-temperature solid-state reaction matched well with protoenstatite phase $MgSiO_3$ crystals (ICSD 36262) (Fig. 1b), confirming the orthorhombic *Pbcn* symmetry. The monotonic shift of diffraction peaks toward larger angles with increasing Cr^{3+} content indicates the successful incorporation of Cr^{3+} (0.64 Å, CN = 6) into the larger Mg^{2+} (0.72 Å, CN = 6) sites. Detail structural information was obtained through Rietveld refinement (Fig. 1c and Supplementary Fig. 2). The refined structural parameters of $MgSiO_3$:*x*%Cr,Li are listed in Supplementary Table 1. The lattice parameters *a*, *b*, and *c* decrease nearly linearly with increasing Cr^{3+} concentration (Fig. 1d), demonstrating that Cr^{3+} preferentially occupies Mg^{2+} sites rather than being oxidized to Cr^{4+} at Si^{4+} sites[12].

X-ray photoelectron spectroscopy (XPS) was employed to preliminarily identify the elemental composition and valence state of Cr in $MgSiO_3$:Cr,Li (Supplementary Fig. 3). The survey spectra confirm the co-existence of all target elements. The Cr $2p_{3/2}$ and $2p_{1/2}$ peaks centered at binding energies of 578.0 and 587.2 eV are characteristic of trivalent Cr^{3+}, with no detectable contribution from tetravalent Cr[22]. ^{7}Li solid-state nuclear magnetic resonance (NMR) spectroscopy was performed to confirm the incorporation of Li (Fig. 1e). Rotation side-bands are marked with asterisks. The NMR spectrum of $MgSiO_3$:Cr,Li shows one sharp isotropic signal, confirming the incorporation of Li^+ ions into the $MgSiO_3$ framework[6, 23]. The doped Li^+ ions occupy the Mg^{2+} sites within the crystal lattice, with no evidence of interstitial Li^+ ions being observed[13]. Scanning electron microscopy (SEM) image reveals irregular micrometer-sized grains of the as-synthesized $MgSiO_3$:Cr,Li with a homogeneous distribution of Mg, Si, O, and Cr across individual particles (Fig. 1f and Supplementary Fig. 4a). Energy dispersive spectroscopy (EDS) further confirms that the element ratios of Mg, Si, O and Cr are consistent with the nominal stoichiometry (Supplementary Fig. 4b). High-resolution transmission electron microscopy (HR-TEM) image demonstrates the high crystallinity of the sample, exhibiting well-defined (121) lattice fringe with an interplanar spacing of 0.327 nm (Fig. 1g). Atomic-resolution high-angle dark-field scanning transmission electron microscopy (HAADF-STEM) imaging of $MgSiO_3$:Cr,Li phosphor (Fig. 1h) reveals cation arrangements consistent with the projection along $[10\ \bar{1}]$ zone axis of the protoenstatite phase crystallized in the orthorhombic system within *Pbcn* space group (Fig. 1i). Brighter points in the image correspond to overlapping Mg and Si atomic columns, while darker points correspond to non-overlapping atoms. The uniformly ordered cation arrangement confirms the preservation of the protoenstatite framework with excellent crystallinity. Simulated HAADF- STEM image (Fig. 1k) and electron-diffraction pattern (Fig. 1l), generated based on the constructed *Pbcn* stacking structure model along the $[10\ \bar{1}]$ zone axis, agree closely with experimental observations (Fig. 1i-j), further validating the crystal structural assignment.

Figure 2a shows the room-temperature PL and PLE spectra of $MgSiO_3$:2%Cr,Li. When monitored at 880 nm, three broad excitation bands centered at 298, 450 and 640 nm are observed, corresponding to the spin-allowed $^4A_2 \rightarrow {}^4T_1$ (^4P), $^4A_2 \rightarrow {}^4T_1$ (^4F) and $^4A_2 \rightarrow {}^4T_2$ (^4F) transitions of Cr^{3+}, respectively[24, 25]. A weak shoulder near 680 nm is attributed to the spin-forbidden $^4A_2 \rightarrow {}^2E_g$ (^2G) transition. Upon 450 nm excitation, $MgSiO_3$:2%Cr,Li exhibits broadband NIR emission peaking at 880 nm, covering the 700–1200 nm spectral region. This emission originates from the $^4T_2$ (^4F) → $^4A_2$ transition of Cr^{3+} [26]. To determine the optimal activator concentration, a series of MgSiO3:*x*%Cr,Li (*x* = 0.25–2.5) samples were synthesized for a comprehensive examination of structural and luminescent properties. The diffuse reflection spectra (DRS) of Cr^{3+} doped samples display pronounced absorption bands in the blue and red visible regions, assigned to the $^4A_2 \rightarrow {}^4T_1$ (^4F) and $^4A_2 \rightarrow {}^4T_2$ (^4F) transitions (Supplementary Fig. 5). The excitation bands in the PLE spectra agree well with DRS, and no characteristic absorption of Cr^{4+} are detected. The optical band gap (E_g) of $MgSiO_3$:Cr,Li, determined by the Tauc plot method derived from Kubelka–Munk transformed reflectance data, is approximately 4.71 eV (Supplementary Fig. 6). This wide E_g ensures that the $^4T_1$ and $^4T_2$ excited levels remain well separated from the conduction band, suppressing potential photoionization process induced thermal quenching[27].

Figure 2b presents the normalized PL spectra of $MgSiO_3$:*x*%Cr,Li (*x* = 0.25–2.5). With increasing Cr^{3+} concentration, the emission maximum gradually redshifts from 865 to 885 nm. The integrated PL intensity increases initially, reaches a maximum at 2 mol% Cr^{3+}, and subsequently decreases due to concentration quenching (Fig. 2c). Interestingly, the NIR emission bandwidth (FWHM) narrows progressively with increasing Cr^{3+} content. This behavior deviates from the conventional broadening caused by enhanced electron–phonon coupling at high dopant concentrations. This anomalous spectral evolution suggests the presence of multiple luminescent centers and possible inter-site energy transfer. The *Pbcn*-phase $MgSiO_3$ lattice contains two crystallographically independent Mg sites (Mg1 and Mg2), providing the structural basis for dual-site occupation of Cr^{3+}. The emission spectra of low concentration doped samples (*x* = 0.25–1) can be well fitted with twocomponents. This anomalous spectral evolution indicates the presence of multiple emitting species and directional inter-site energy transfer (Supplementary Fig. 7a–c). At 80 K, distinct double emission bands centered at ~ 730 nm and ~ 848 nm are observed for $MgSiO_3$:0.25%Cr,Li upon both 430 and 450 nm excitation, providing direct spectroscopic evidence for dual-site occupation (Fig. 2d, top). According to crystal-field theory, the crystal field splitting energy (D_q) decreases with increasing metal–ligand distance ($D_q \propto R^{-5}$) [28]. Structural analysis shows that the [$Mg1O_6$] octahedron exhibits longer average Mg–O bond lengths and a larger polyhedral distortion index than [$Mg2O_6$], indicating a weaker crystal field at the Mg1 site. Therefore, Cr^{3+} ions occupying Mg1 (denoted Cr1) emit at longer wavelengths, while those at Mg2 (Cr2) experience a stronger crystal field and emit at shorter wavelengths. The site assignment is further supported by lifetime differences, with Cr1 exhibiting shorter decay times due to its smaller energy gap. As the Cr^{3+} concentration increases, the relative contribution of Cr2 emission diminishes progressively, and at concentrations above 1.5 mol%, only a single broadband NIR emission band centered near 865–885 nm

is observed at room temperature (Supplementary Fig. 7d–f). Even in $MgSiO_3$:2%Cr,Li, where only one emission band appears at 80 K, PLE spectra monitored at 730 nm and 865 nm display distinct excitation profiles (Fig. 2d, bottom), confirming the coexistence of two Cr^{3+} centers. These observations indicate efficient non-radiative energy transfer from the higher-energy Cr2 centers to the lower-energy Cr1 centers. Time-resolved photoluminescence measurements of the dominant Cr1 emission reveal a non-monotonic concentration dependence that reflects the evolution of inter-site energy migration. As the Cr^{3+} concentration increases from 0.25 to 1.0 mol%, the average lifetime (calculated on the basis of Supplementary Eq. (6–**7**)) of the Cr1 center increases progressively, reaching a maximum at x = 1.0 (Supplementary Fig. 8). This lifetime elongation is accompanied by a concomitant shortening of the Cr2 lifetime (Supplementary Fig. 9), providing direct kinetic evidence for an activated Cr2→Cr1 energy funneling regime. This regime enhances the radiative population of Cr1 centers, leading to a concurrent increase in internal quantum efficiency (IQE) from 86.5% to a maximum of 97.3% (Supplementary Fig. 10). Beyond x = 1.0, the Cr1 lifetime decreases due to concentration-induced non-radiative interactions, accompanied by a gradual IQE reduction (to 92.9% at x = 2.5), marking the onset of concentration quenching. In parallel, the gradual redshift of the Cr^{3+} emission correlates with concentration-dependent crystal-field modulation. Rietveld refinement reveals a slight elongation of the average Mg1–O bond length with increasing Cr^{3+} concentration, accompanied by a monotonic decrease in the D_q/B ratio calculated by Supplementary Eq. (1–4) (Supplementary Fig. 11). According to the Tanabe–Sugano diagram for the d^3 configuration of Cr^{3+}, a reduced D_q/B corresponds to a reduced energy gap between the $^4T_2$ and $^4A_2$ states, resulting in a redshifted $^4T_2 \rightarrow {}^4A_2$ transition[29]. These correlations confirm that the observed spectral evolution originates from energy transfer and crystal field modulation induced by local lattice evolution around the Cr^{3+} ions.

Targeted regulation of the local structure of the octahedra hosting the activator Cr^{3+} ions is essential for maximizing NIR luminescence efficiency. By systematically adjusting the Li^+ content, we finely modulate the distortion of the [$Mg1O_6$] octahedra hosting the dominant Cr1 centers responsible for the ~ 880 nm emission. Potential effects on local structure upon Li^+ were investigated using XRD-Rietveld refinement (Supplementary Fig. 12). Detailed structural parameters of $MgSiO_3$:Cr,y%Li are listed in Supplementary Table 2. Diffuse reflection spectra (DRS) illustrate the visible-light absorption of Cr^{3+} increases markedly with Li^+ incorporation (Fig. 2e). This enhancement originates from Li^+-induced local structure distortion: the distortion index of the [$Mg1O_6$] octahedra increases from 4.78% to 7.53% with rising Li^+ content (Fig. 2f, top). The distortion index was calculated using the bond length data in Supplementary Table 3 and Supplementary Eq. (5). The increased asymmetry partially relaxes the Laporte-forbidden rule of Cr^{3+} d–d transitions, thereby enlarging the absorption cross-section without increasing Cr^{3+} concentration. In addition to enhancing absorption, Li^+ incorporation modifies inter-site interactions. Structural refinement indicates that as Li^+ content increases, the average Mg1–Mg2 distance gradually decreases (Fig. 2f, bottom), which shortens the spatial separation between Cr1 and Cr2 centers and facilitates Cr2→Cr1 energy transfer. As a result, the emission bandwidth gradually narrows to ~ 2,061 cm^{-1} (~ 160 nm) at the

optimal Li^+ concentration (Fig. 2g), consistent with more efficient energy funneling toward the energetically favorable Cr1 centers. To elucidate the site preferences of Li^+ and Cr^{3+}, density functional theory (DFT) calculations were performed for four possible substitution configurations in the *Pbcn*-phase $MgSiO_3$ lattice (Supplementary Fig. 13). All configurations exhibit negative formation energies: Cr→Mg2 + Li→Mg2 (-9.13 eV), Cr→Mg2 + Li→Mg1 (-9.19 eV), Cr→Mg1 + Li→Mg2 (-10.21 eV), and Cr→Mg1 + Li→Mg1 (-9.56 eV), indicating thermodynamic feasibility of occupation at either Mg site. Notably, the gradual elongation of Mg2–O bonds with increasing Li^+ content implies preferential Li^+ substitution at Mg2 sites (Supplementary Fig. 14). Meanwhile, the nearly invariant Mg1–O bond length preserves the crystal-field strength at Cr1 centers, explaining why the emission peak position remains essentially unchanged with varying Li^+ content (Fig. 2g). The cooperative redistribution of Li^+ and Cr^{3+} among Mg sites therefore stabilizes the Cr1 emission energy while enhancing structural asymmetry. Consequently, the luminescence intensity of $MgSiO_3$:Cr,*y*%Li increases steadily with Li^+ concentration, reaching a maximum at y = 6.5, then slightly decreases due to excessive lattice distortion potentially promoting non-radiative relaxation.

To gain deeper insight into the broadband NIR luminescence mechanism, electron paramagnetic resonance (EPR) was employed to probe the local environment of the paramagnetic Cr^{3+} ion. The low-field region displays strong resonances at g = 3.70, 4.4, and 4.7, along with weak resonances at g = 2.5, 2.8 and 5.5, suggesting the coexistence of multiple isolated Cr^{3+} centers in distorted octahedral sites primarily subjected to axial crystal fields (Supplementary Fig. 15).[30] A weak high-field resonance at g = 1.95 suggests only a limited presence of exchange-coupled Cr^{3+}–Cr^{3+} pairs. As Cr^{3+} concentration increases, the intensity of isolated-center signals increases proportionally, while exchange-coupled features remain weak, indicating that broadband NIR emission is primarily governed by isolated Cr^{3+} centers rather than clustered pairs. Importantly, increasing Li^+ content further enhances the low-field isolated Cr^{3+} signals, suggesting that Li^+ incorporation both suppresses defect formation and strengthens local distortion around isolated Cr^{3+} ions. Collectively, these results suggest that the broadband NIR emission arises from the cooperative contribution of multiple isolated Cr^{3+} centers and inter-site energy transfer pathways, with Li^+ incorporation providing effective structural regulation to optimize radiative efficiency. This observation aligns with the absorption enhancement and improved radiative efficiency discussed above.

EQE serves as a crucial metric for evaluating the performance of NIR phosphors. All $MgSiO_3$:Cr,*y*%Li samples exhibit high internal quantum efficiencies (IQE) with excellent EQE of exceeding 56.4% (Fig. 2h). The absorption efficiency (AE) at 450 nm increases significantly with Li^+ content, directly reflecting Li^+-induced relaxation of parity-forbidden *d*–*d* transitions. Importantly, this enhancement is achieved without increasing Cr^{3+} concentration, thereby avoiding the concentration quenching that typically limits conventional Cr^{3+}-activated phosphors. The optimized composition achieves an EQE of 64% at λ_{max} ~ 880 nm. Figure 2i summarizes the EQE and peak emission wavelengths of representative Cr^{3+}-activated NIR phosphors and $MgSiO_3$:Cr,Li. The indexed materials are listed in Supplementary Table 4. Notably,

$MgSiO_3$:Cr,Li simultaneously achieves low-energy emission (~ 880 nm) with the highest reported EQE (64%) among Cr^{3+}-based broadband NIR phosphors to date. Moreover, its emission portion extends into the short-wave infrared region, making it suitable for practical applications in broadband NIR illumination systems. Collectively, these results demonstrate that Li^+-mediated local structural engineering simultaneously enhances the optical absorption, optimizes inter-site energy transfer, preserves favorable crystal-field strength, and suppresses the defect-related losses, thereby establishing $MgSiO_3$:Cr,Li as a highly efficient NIR phosphor platform.

To assess the suitability of $MgSiO_3$:Cr,Li as a broadband NIR emitter for practical operation, its thermal and chemical stability were systematically evaluated. Variable-temperature XRD measurements reveal no detectable phase transition between 83 and 423 K, indicating the structural robustness of the protoenstatite framework over a wide temperature range (Fig. 3a). Temperature-dependent PL spectra of representative sample upon 450 nm excitation show only a gradual intensity decrease and a slight redshift with increasing temperature (Fig. 3b). The redshift of Cr^{3+} emission results from temperature-induced lattice expansion, which weakens the crystal field strength and lowers the $^4T_2 \rightarrow {}^4A_2$ transition energy of Cr^{3+}. As shown in Fig. 3c, the integrated radiation intensity retained 77% of its room-temperature value at 423 K, highlighting its robustness across a broad temperature range. Luminescent thermal quenching behavior can be visualized via the schematic configuration coordinate diagram (Fig. 3d), where non-radiative relaxation occurs via thermally activated crossover between the $^4T_2$ and $^4A_2$ states[31]. Arrhenius analysis, fitting the integrated PL spectral intensity using Supplementary Eq. (8), yields an activation energy (ΔE) of 0.092 eV (Fig. 3e), indicating a sufficiently high barrier against non-radiative recombination. Furthermore, the relationship between electron-phonon coupling effect and thermal stability was evaluated using Supplementary Eq. (9)[32]. The temperature-induced weak spectral broadening corresponds to a Huang-Rhys factor (S) value of 1.60 and an effective phonon energy of 0.063 eV, reflecting relatively weak electron–phonon coupling (Fig. 3f). Besides the wide bandgap of protoenstatite (4.7 eV) effectively suppressing thermal ionization processes of excited 3*d* states, the exceptional PL properties benefit from the high structural rigidity, quantified by a high Debye temperature (531 K)[17], which serves as a reliable descriptor for inorganic framework stability[33].

Previous studies have primarily focused on the thermal stability of luminescent materials but neglected their chemical and environmental stability, despite the latter being equally critical for practical applications. Here, representative phosphors were immersed in various liquids to investigate the chemical stability. The XRD patterns show no structural degradation after 7 days of immersion in water, HNO_3 (10% aq.), HCl (10% aq.), NaOH (1 mol L^{-1}) and NaCl (1 mol L^{-1}) (Supplementary Fig. 16). Following immersion, the samples still emit bright NIR light upon blue light excitation, with consistent spectral shapes in the 700–1200 nm range (Fig. 3g). The loss in luminescence intensity after 7 days of soaking was negligible compared to the pristine, indicating the excellent chemical stability of $MgSiO_3$:Cr,Li (Fig. 3h). Furthermore, the phosphor was exposed to high temperature (85°C) and relative humidity (85% RH) to simulate the effect of extreme environment on luminescence performance. The

spectral shape remains consistent during aging, with NIR brightness retaining 98% of its initial value after 7 days of aging (Fig. 3i). The luminescence of $MgSiO_3$:Cr,Li exhibits robustness under harsh conditions such as strong acids, strong bases, high temperatures, high humidity, and high salinity, underscoring the material's significant potential as an efficient broadband NIR light source under extreme environments.

As a proof of concept, the optimized $MgSiO_3$:Cr,Li phosphor was integrated onto a commercial 450 nm chip-on-board (COB) blue LED as a light-conversion layer to fabricate a NIR pc-LED. Figure 4a presents the electroluminescence (EL) spectra recorded under injection currents from 20 to 1600 mA. With increasing drive current, the EL intensity rises while the spectral shape remains unchanged, consisting of two emission bands originating from the blue LED (~ 450 nm) and the Cr^{3+}-activated phosphor (~ 880 nm). The device exhibits exceptional electro-optical conversion enabled by the high EQE of the $MgSiO_3$:Cr,Li phosphor. The conversion efficiency from electrical input power to NIR output ($\eta_{NIR/Input}$) reaches 27.96% at 20 mA and gradually decreased to 18.15% at 1600 mA, mainly due to the efficiency roll-off of the blue LED and thermal quenching of the phosphor caused by chip heating at high current operation (Fig. 4b). Similarly, the blue-to-NIR conversion efficiency ($\eta_{NIR/Blue}$) decreases slightly from a maximum of 40.99% to 37.67% as the injection current increases. Despite this moderate efficiency reduction, the NIR radiant output increases markedly from 0.04 to 2.77 W as the current rises from 20 to 1600 mA, demonstrating high-power NIR generation (Fig. 4c). Additionally, to further evaluate device scalability, the phosphor was also applied to miniature (2.8 × 3.5 mm) 450 nm surface-mounted-devices (SMD) LED. This device exhibits a record maximum electro-optical conversion efficiency of 32.91% at 10 mA and an NIR output power of 162 mW at 300 mA, indicating suitability for compact NIR light sources (Supplementary Fig. 18). The detailed parameters for the two as-fabricated devices are summarized in Supplementary Tables 5 and 6. The obtained output power and photoconversion efficiency surpass those of commercially available NIR LEDs such as OSLON P1616 SFH 4737 (Osram, Germany) and LUXEON IR ONYX (Lumileds, USA), as well as previously reported NIR pc-LEDs[8, 34]. Thermal imaging confirms stable device operation at elevated currents, with a maximum surface temperature of 118.1°C at 1600 mA (Supplementary Fig. 17). At this temperature the phosphor still retains substantial emission intensity, reflecting the good thermal tolerance of the $MgSiO_3$:Cr,Li system and the effective heat dissipation of the COB architecture. Operational stability was assessed through cyclic and continuous testing. Under repeated switching at 1000 mA, the emission spectra remain unchanged (Fig. 4d), and the integrated NIR output intensity retains 99.05% of its initial value after 2435 cycles (Fig. 4e). Continuous operation at 1000 mA for 100 h also shows negligible degradation in NIR emission intensity (Fig. 4f). These results demonstrate the excellent operational stability of the fabricated NIR pc-LED and highlight the potential of $MgSiO_3$:Cr,Li phosphor for high-power NIR optoelectronic applications.

Figure 4g illustrates the structural configuration of the packaged NIR light source. The NIR emission generated by the pc-LED is first collimated by an aluminum reflector cup and subsequently filtered through a long-pass optical filter to produce broadband NIR illumination. An aluminum heat sink equipped with a cooling fan serves both as the thermal management component and as the mechanical

support for the device. Upon operation, the assembled light source emits intense broadband NIR radiation capable of illuminating a corridor approximately 40 m in length (Fig. 4h). Clear NIR images captured by the experimenter at a distance of 40 m demonstrate the long-range night-vision imaging capability enabled by the high radiant output of the developed NIR pc-LED system (Fig. 4i). Benefiting from the reduced scattering and high penetration depth of NIR light in biological tissues, the high-power source was further employed to demonstrate vascular imaging in transmission mode. Owing to the different absorption characteristics of biological tissues in the NIR region, the contrast in the recorded images corresponds to variations in transmitted NIR intensity, allowing for the differentiation of various anatomical structures. As shown in Fig. 4j-l, NIR light readily penetrates the human finger, palm and wrist, clearly revealing skeletal structures and vascular networks. The watt-level NIR output enables high signal-to-noise imaging with exposure times of only several tens of milliseconds, resolving vascular features ranging from fine capillaries to millimetre-scale arteries and veins.

In conclusion, we demonstrate that precise local structural engineering within a rigid silicate framework enables highly efficient broadband NIR emission. By modulating Li^+ content in Cr^{3+}-activated *Pbcn*-phase $MgSiO_3$ (protoenstatite), the local symmetry and distortion of the Cr^{3+}-coordinating octahedra are selectively regulated, leading to enhanced blue-light absorption through partial relaxation of selection rules and optimized radiative recombination dynamics. The resulting phosphor delivers high external quantum efficiency of 64% at λ_{max} ~ 880 nm together with remarkable thermal and environmental robustness. When integrated with a commercial InGaN chip, it supports watt-level NIR output with excellent operational stability. This work establishes local symmetry manipulation in structurally rigid oxide as a robust strategy for designing high-performance *d*-electron phosphors for next-generation NIR optoelectronics.

Methods

Materials

$MgSiO_3$:*x*%Cr,Li (*x* = 0.25–2.5 mol%) and $MgSiO_3$:Cr,*y*%Li (*y* = 4–7.5 mol%) phosphors were synthesized via a conventional high-temperature solid-state reaction method. High-purity MgO (Aladdin, 99.99%), SiO_2 (Aladdin, ≈ 5 μm, 99.99%), Cr_2O_3 (Aladdin, 99.95%) and Li_2CO_3 (Aladdin, 99.99%) were weighed according to the stoichiometric compositions and thoroughly mixed in anhydrous ethanol. The mixtures were wet-milled for 10 min using a nylon milling jar with zirconia balls as the grinding media. After drying, the homogeneous powders were transferred into alumina crucibles and calcined in air at 1150°C for 6 h with a heating rate of 5°C min^{-1} in a muffle furnace. The obtained products were ground into fine powders and subsequently washed several times with deionized water and dilute hydrochloric acid under ultrasonication to remove potentially residual impurities. The final phosphor powders were dried prior to further characterization.

Fabrication of NIR pc-LED

The optimal $MgSiO_3$:Cr,Li NIR phosphor was mixed with silicone resin (component A:B = 1:4 by weight) in a mass ratio of 3:5. The mixture was thoroughly stirred and degassed under vacuum to remove trapped air bubbles, then coated onto a 450 nm InGaN blue LED chip. The assembled device was subsequently cured at 100°C for 2 h to obtain the NIR pc-LED.

Characterization

Powder X-ray diffraction (XRD) patterns of all samples were collected using a Bruker D8 ADVANCE diffractometer equipped with monochromated Cu Kα radiation (λ = 1.54056 Å) and a LYNXEYE XE-T detector, operated at 40 kV and 40 mA. The XRD data were acquired over a range of 10–80° (2 theta), with a step size of 0.01° and a counting time of 0.3 seconds per step. Temperature-dependent XRD patterns were collected on the same model diffractometer equipped with a low-/high-temperature in situ attachment. Rietveld refinements of the powder XRD data were performed using the FullProf suite. The particle morphology and elemental mapping were characterized using a field-emission scanning electron microscope (FE-SEM, Apreo 2S HiVac, Thermo Fisher Scientific) equipped with an energy-dispersive X-ray spectroscopy system. X-ray photoelectron spectroscopy (XPS) measurements were carried out on an AXIS Supra+ spectrometer (Shimadzu Corporation). The solid-state nuclear magnetic resonance (NMR) spectra of ^{7}Li were recorded on a Bruker Avance Neo 600 MHz NMR spectrometer (Bruker Corporation). High-resolution transmission electron microscopy (HR-TEM) images were acquired using a Talos 200X G2 microscope (Thermo Fisher Scientific). High-angle annular dark-field scanning transmission electron microscopy (HAADF-STEM) images were recorded on a double aberration-corrected transmission electron microscope (JEM-ARM300F2) operated at 300 kV. HAADF-STEM image simulations of the *Pbcn*-phase $MgSiO_3$ structure along the $[10\ \bar{1}]$ zone axis were performed using the Dr. Probe software package[35]. Electron diffraction patterns were simulated using the ReciPro software package[36]. Diffuse reflectance (DR) spectra were measured on a Hitachi UH4150 UV-vis-NIR spectrophotometer using $BaSO_4$ as the reflectance standard. Room-temperature photoluminescence (PL) and photoluminescence excitation (PLE) spectra were recorded on an Edinburgh Instruments FLS1000 spectrofluorometer equipped with a 450 W continuous xenon lamp as the excitation source and a liquid-nitrogen-cooled NIR photomultiplier tube (Hamamatsu R5509-72) as the detector. Temperature-dependent PL spectra were measured using the same spectrometer equipped with a temperature-controlled stage (TS600V-SM). PL decay curves were collected on the same FLS1000 system using a 100 W microsecond flash lamp (μF2) as the excitation source. The PL quantum efficiency of the phosphors was measured at room temperature using a Quantaurus-QY Plus C13534-12 absolute quantum yield spectrometer (Hamamatsu Photonics). Electron paramagnetic resonance (EPR) spectra were measured at room temperature using a Bruker Magnettech ESR5000 X-band spectrometer operating at 9.45 GHz. The electroluminescence performance of the fabricated NIR pc-LED was characterized using an ATA-500 optoelectronic measurement system (EVERFINE) equipped with a HAAS-2000 spectroradiometer. Visible images were captured using an iPhone 16 Pro, and NIR images were obtained with a short-wave infrared camera

(SWIR330KMB-UMV). The operating temperature of NIR pc-LED was monitored using a FLIR C5 thermal imaging camera.

Computational procedure

Several 2×2×1 supercells of *Pbcn*-phase $MgSiO_3$ were built to fit the simulated experimental facts, and simulations were performed using the Vienna ab initio simulation package with projector augmented plane-wave method within the density functional theory framework[37, 38]. The generalzied proposed by Perdew, Burke, and Ernzerhof is selected for the exchange-correlation potential[39]. The cut-off energy for plane wave is set to 520 eV. The relaxation energy convergence was set at 1×10^{-5} eV per atom. All the structures are relaxed until the residual forces on the atoms have declined to less than 0.01 eV/Å. K-point meshes with a resolution of $2\pi \times 0.03$ $Å^{-1}$ were adopted for integration in the Brillouin zone for geometric optimization. The defect formation energies (E_f) for different types of Cr and Li doped $MgSiO_3$ were calculated using the following formula:

$$E_f = E(\text{doped}) - E(\text{pure}) - \sum n_i \mu_i$$

1

where E(doped) and E(pure) are the total energy of the doped and undoped crystal, respectively. n_i and μ_i represent the chemical potential and the number of the added ($n_i > 0$) or removed ($n_i < 0$) *i*-type atoms, respectively.

Declarations

Author Contributions Statement

L. Zhong, Y. Xiang, Z. Wu and C. Jiang synthesized the materials and performed the characterization; L.Zhong, J. Tang and S. Rao curated the data; L. Zhong, C. Jiang and L. Zhou wrote the original draft; L. Zhou, X. J. Wang and M. Wu supervised the project.

Acknowledgements

This work was supported by the National Natural Science Foundation of China (NSFC) (Nos. 52272174, 52572189, 52002411) and its joint project with Guangdong Province (Nos. U22A20135). Lei Zhou acknowledges the support of the Southern Marine Science and Engineering Guangdong Laboratory (Zhuhai) (311024020). The work has also been supported by bilateral project China-Serbia, and Oceano Company for new phosphors.

Data availability

The data that support the findings of this study are available from the corresponding author on reasonable requests.

References

1. Sun Y et al (2023) Bright and stable perovskite light-emitting diodes in the near-infrared range. Nature 615:830–835
2. Liu G et al (2024) Laser-driven broadband near-infrared light source with watt-level output. Nat Photonics 18:562–568
3. Yuan F et al (2024) Bright and stable near-infrared lead-free perovskite light-emitting diodes. Nat Photonics 18:170–176
4. Liu S et al (2026) Chromium-activated phosphors: from theory to applications. Chem Soc Rev 55:1954–1998
5. Chen K-C et al (2026) Revolutionary near-infrared phosphors with emerging structures and mechanisms driving next-generation applications. Prog Mater Sci 157:101588
6. Pust P et al (2014) Narrow-band red-emitting $Sr[LiAl_3N_4]:Eu^{2+}$ as a next-generation LED-phosphor material. Nat Mater 13:891–896
7. Fang Y et al (2026) Deep-penetrating mechano-optics: autonomous NIR signaling for bio-implant surveillance. Mater Today 93:103208
8. Zheng G et al (2025) Rare-metal-free ultrabroadband near-infrared phosphors. Adv Mater 37:2415791
9. Jiang L et al (2024) Awakening the dumb site to realize ultra-broadband NIR phosphor. Laser Photonics Rev 18:2301226
10. Xiao W et al (2023) Suppressed concentration quenching brightens short-wave infrared emitters. Adv Mater 35:2306517
11. Basore ET et al (2024) Unveiling suppressed concentration quenching enhanced broadband near-infrared emitters. ACS Appl Mater Interfaces 16:65068–65076
12. Zhong L et al (2025) Valence and site engineering enable efficient broadband near-infrared emission at 960 nm in Cr^{3+}-activated forsterite. Adv Mater 37:2508768
13. He F et al (2022) Interstitial Li^+ occupancy enabling radiative/nonradiative transition control toward highly efficient Cr^{3+}-based near-infrared luminescence. ACS Appl Mater Interfaces 14:31035–31043
14. Liu G, Xia Z (2022) Modulation of thermally stable photoluminescence in Cr^{3+}-based near-infrared phosphors. J Phys Chem Lett 13:5001–5008
15. Deng J et al (2026) The potential for bridgmanite megacrysts to drive magma ocean segregation. Nature 650:361–366

16. Reid AM et al (1964) Luminescence of orthopyroxenes. Nature 204:1292–1293
17. Zhuo Y et al (2018) Identifying an efficient, thermally robust inorganic phosphor host via machine learning. Nat Commun 9:4377
18. Lin L et al (2006) Synthesis and luminescence properties of red phosphors: Mn^{2+} doped $MgSiO_3$ and Mg_2SiO_4 prepared by sol-gel method. J Rare Earths 24:104–107
19. Fang J et al (2024) Harnessing Cu incorporation for achieving stable superior microwave dielectric properties in low permittivity $MgSiO_3$-based ceramics through effective phase transition suppression. Ceram Int 50:38357–38364
20. Ashbrook SE et al (2007) O and ^{29}Si NMR parameters of $MgSiO_3$ phases from high-resolution solid-state NMR spectroscopy and first-principles calculations. J Am Chem Soc 129 17:13213–13224
21. Ghose S et al (1994) Lattice dynamics and Raman spectroscopy of protoenstatite $Mg_2Si_2O_6$. Phys Chem Min 20:469–477
22. Wang X et al (2026) Cr^{3+}-activated tunable near-infrared mechanoluminescence materials for potential water pollutant monitoring. Adv Funct Mater 36:e15717
23. Wang P et al (2025) Enhanced stability and brightness through co-substitution: Promoting plant growth with green-excited deep red phosphor $Ca_{1-z}Sr_zLi_{1-x}Mg_{2x}Al_{3-x}N_4:yEu^{2+}$. Adv Mater 37:2414578
24. Yan J et al (2025) Novel Cr^{3+}-activated $SrLu_2Ga_{1.5}Al_{2.5}SiO_{12}$ garnet-type near-infrared phosphor: synthesis, luminescence and applications. Mater Today Chem 47:102858
25. Wang Q et al (2022) Efficient Cr^{3+}-activated $NaInP_2O_7$ phosphor for broadband near-infrared LED applications. Inorg Chem Front 9:3692–3701
26. Wang Y et al (2025) High-temperature negative-thermal-quenching in broadband NIR light-emitting $ScF_3:Cr^{3+}$ phosphors. Adv Opt Mater 13:e01552
27. Zhou Z et al (2022) Anti-thermal-quenching, color-tunable and ultra-narrow-band cyan green-emitting phosphor for w-LEDs with enhanced color rendering. Chem Eng J 433:134079
28. Wei M et al (2026) Breaking the absorption-efficiency paradigm: 270% EQE gain in Cr^{3+}-doped phosphors via crystal field engineering. Laser Photonics Rev e02794
29. Song Z et al (2024) Host dependency of boundary between strong and weak crystal field strength of Cr^{3+} luminescence. J Phys Chem Lett 15:2319–2324
30. Lim JX et al (2026) Neutron-resolved double spinel host engineering for ultra-broadband NIR luminescence and Cr^{3+}, Ni^{2+} energy transfer. Adv Funct Mater 36:e16714
31. Zhong L et al (2022) Dual-mode optical thermometry based on intervalence charge transfer excitations in Tb^{3+}/Pr^{3+} co-doped $CaNb_2O_6$ phosphors. Ceram Int 48:30005–30011
32. Li Z et al (2024) High-performance NIR emission in chromium-doped garnet phosphors enabled by structure and excitation regulation. Laser Photonics Rev 18:2300732

33. Brgoch J et al (2013) Proxies from ab initio calculations for screening efficient Ce^{3+} phosphor hosts. J Phys Chem C 117:17955–17959
34. Wang S et al (2023) Achieving high quantum efficiency broadband NIR $Mg_4Ta_2O_9:Cr^{3+}$ phosphor through lithium-ion compensation. Adv Mater 35:e2300124
35. Barthel J (2018) Dr. Probe: A software for high-resolution STEM image simulation. Ultramicroscopy 193:1–11
36. Seto Y, Ohtsuka M (2022) ReciPro: free and open-source multipurpose crystallographic software integrating a crystal model database and viewer, diffraction and microscopy simulators, and diffraction data analysis tools. J Appl Crystallogr 55:397–410
37. Kresse G, Joubert D (1999) From ultrasoft pseudopotentials to the projector augmented-wave method. Phys Rev B 59:1758–1775
38. Kresse G, Furthmüller J (1996) Efficiency of ab-initio total energy calculations for metals and semiconductors using a plane-wave basis set. Comput Mater Sci 6:15–50
39. Perdew JP et al (1996) Generalized gradient approximation made simple. Phys Rev Lett 77:3865–3868

Figures

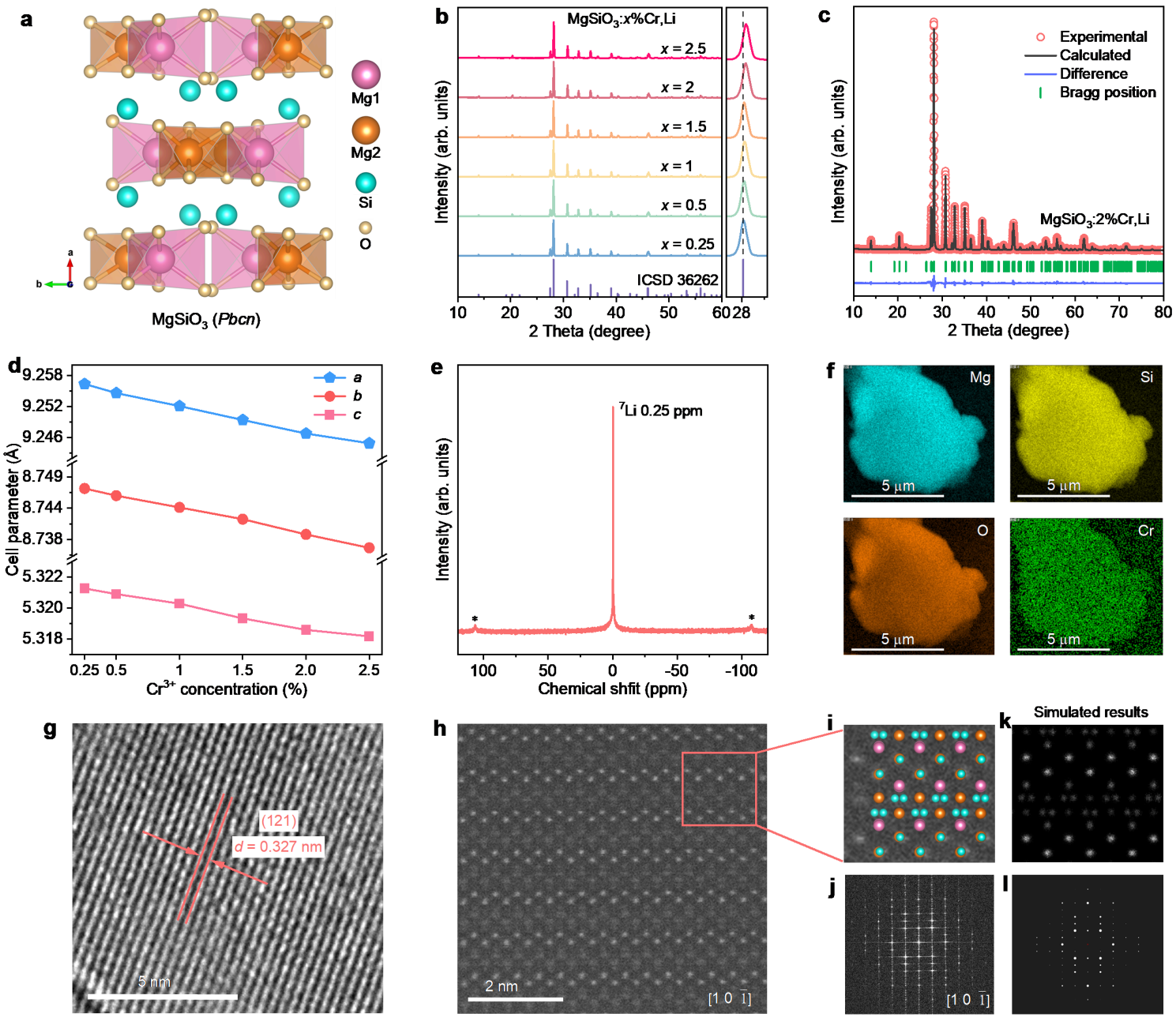


Figure 1

Structure and morphology characterization of $MgSiO_3$:Cr,Li. a Crystal structure diagram of protoenstatite phase $MgSiO_3$. **b** XRD patterns of $MgSiO_3$:*x*%Cr,Li. **c** Rietveld refinement plot of $MgSiO_3$:2%Cr,Li. **d** Variations of cell parameters with different Cr^{3+} doping concentrations. **e** ^7Li solid-state NMR spectrum of $MgSiO_3$:Cr,Li (rotation frequency 25 kHz). **f** Elements mapping images of $MgSiO_3$:2%Cr,Li sample. **g** High-resolution TEM image of $MgSiO_3$:Cr,Li. **h-i** Atomic-resolution HAADF-STEM image and schematic diagram of atomic structure projection along the $[10\bar{1}]$ zone axis. **j** FFT pattern. **k-l** Simulated HAADF-STEM image and electron-diffraction pattern based on the *Pbcn*-phase $MgSiO_3$ crystal structure.

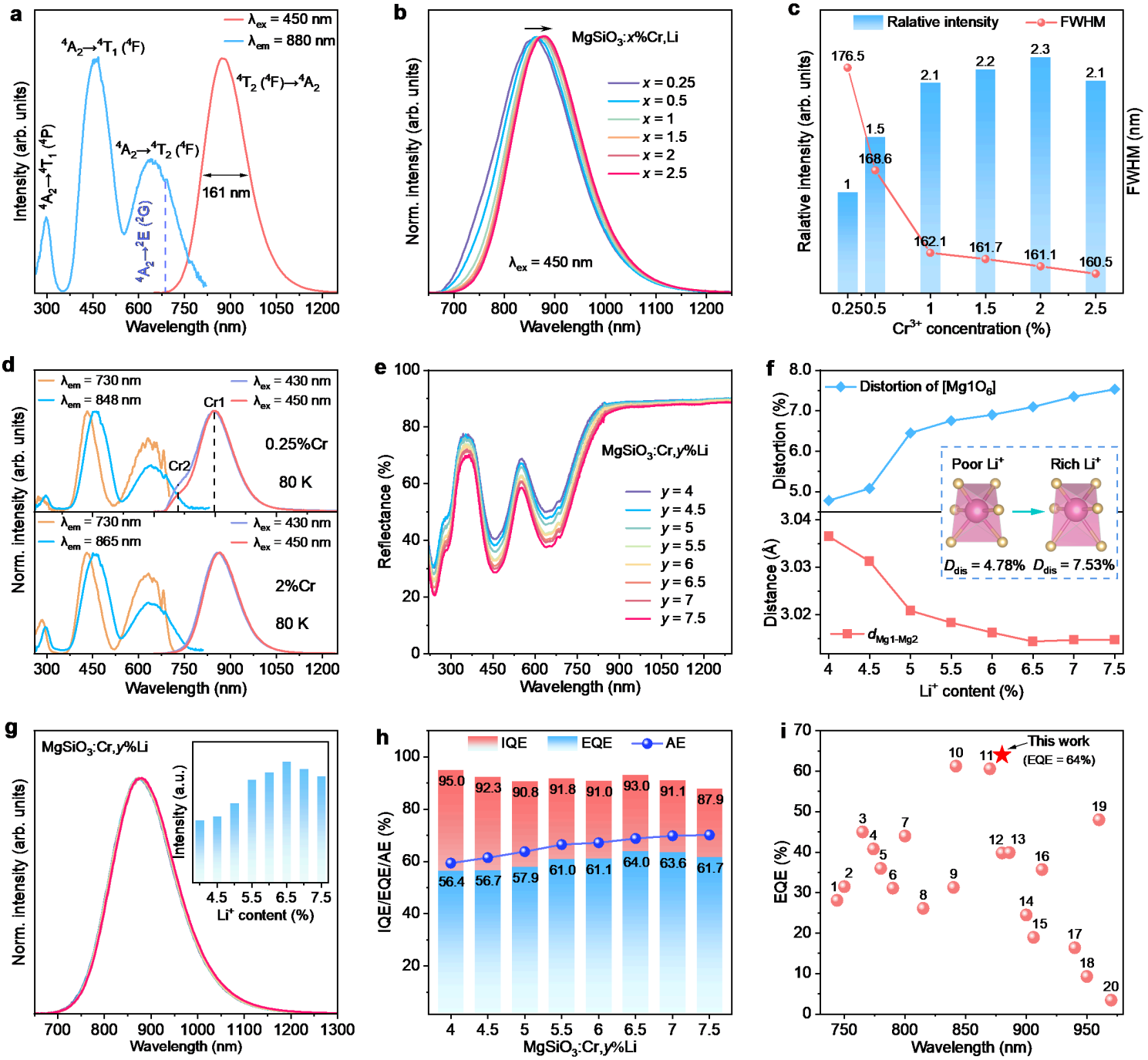


Figure 2

Photoluminescence properties of $MgSiO_3$:Cr,Li phosphors. a photoluminescence emission (PL) and excitation (PLE) spectra of $MgSiO_3$:2%Cr,Li excited at 450 nm and monitored at 880 nm. **b** Normalized PL spectra of $MgSiO_3$:*x*%Cr,Li. **c** Integrated emission intensity and FWHM of $MgSiO_3$:*x*%Cr,Li as a function of Cr^{3+} concentration. **d** PLE and PL spectra of $MgSiO_3$:0.25%Cr,Li and $MgSiO_3$:2%Cr,Li at 80 K. **e** DRS of $MgSiO_3$:Cr,*y*%Li. **f** Distortion of the [$Mg1O_6$] octahedron and the Mg1−Mg2 distance with different Li^+ contents. **g** Normalized PL spectra of $MgSiO_3$:Cr,*y*%Li upon 450 nm excitation. **h** Absolute quantum

efficiencies of $MgSiO_3$:Cr,*y*%Li. **i** EQE of $MgSiO_3$:Cr,Li compared with other Cr^{3+}-doped broadband NIR phosphors excited by blue light.

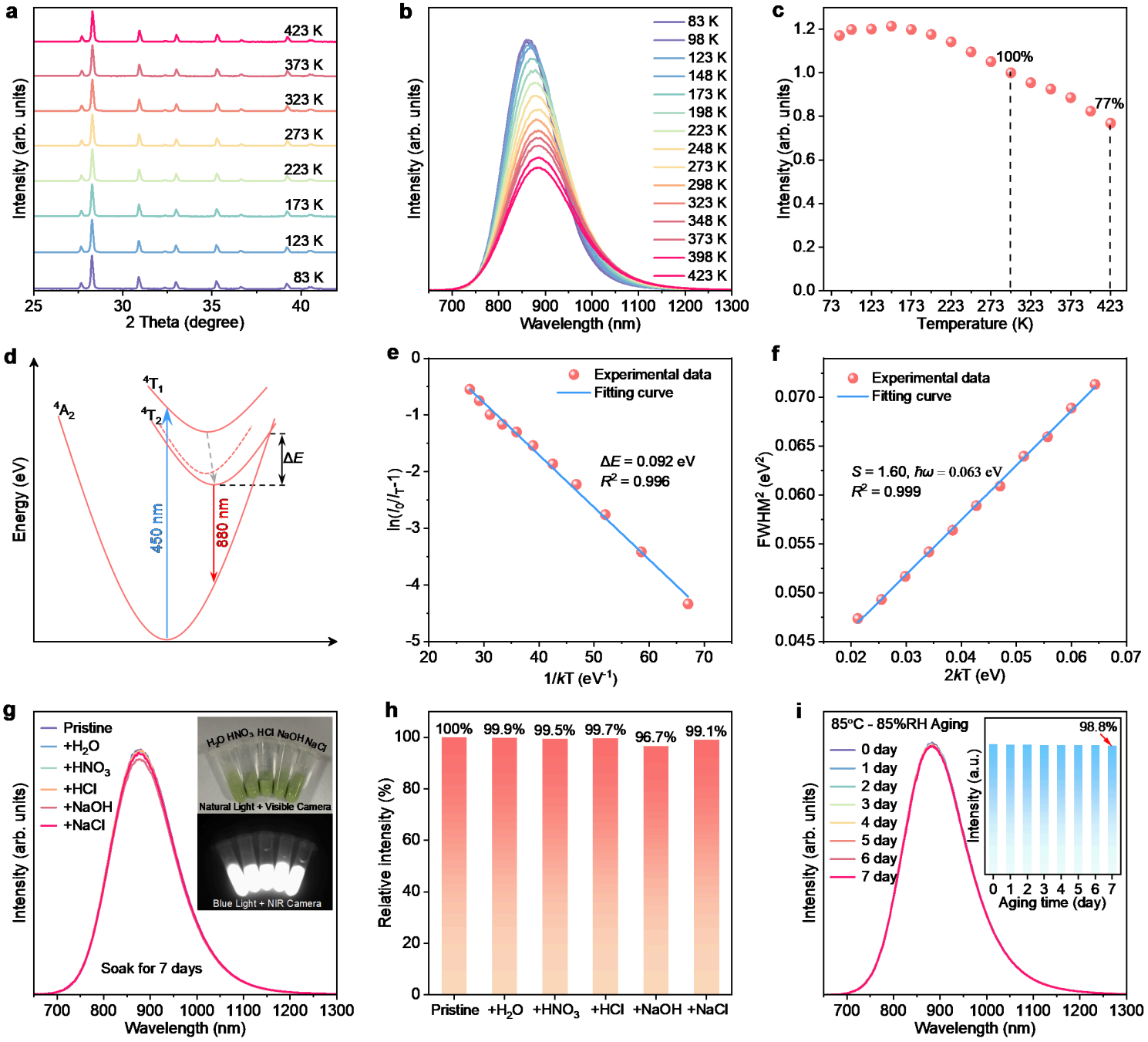


Figure 3

Thermal and chemical stability of $MgSiO_3$:Cr,Li. a Temperature-dependent XRD patterns of $MgSiO_3$:Cr,Li. **b** Temperature-dependent PL spectra. **c** Relative integrated luminescence intensity versus temperature. **d** Configurational coordinate diagram. **e** Plots of $\ln(I_0/I_T - 1)$ versus $1/kT$. **f** The fitting result of Huang-Rhys factor (S) as a function of $2kT$. **g** PL spectra and **h** Relative PL intensity of $MgSiO_3$:Cr,Li phosphors before (pristine) and after 7 days of soaking in H_2O, HNO_3 (10% aq.), HCl (10% aq.), NaOH (1 mol L^{-1}) and NaCl

(1 mol L^{-1}). **i** PL spectra of $MgSiO_3$:Cr,Li phosphors after aging at 85°C and 85% relative humidity for different times.

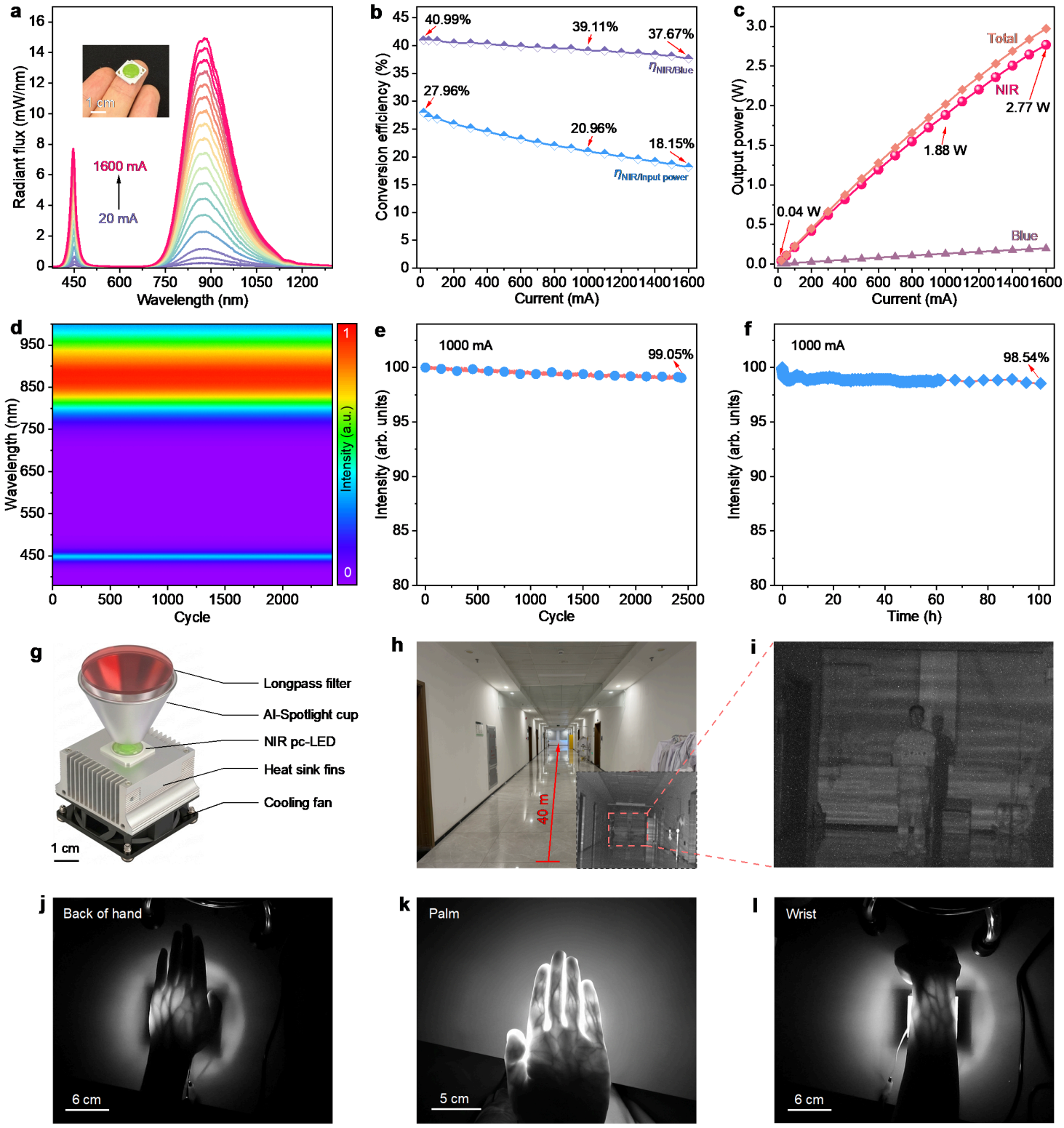


Figure 4

Luminescence properties and applications of NIR pc-LED device. **a** Driven current-dependent emission spectra of the fabricated NIR pc-LED and the inset shows the photograph of the as-fabricated pc-LED

device captured by visible camera. **b** Electro-optical conversion efficiency and blue-to-NIR light conversion efficiency versus driving currents. **c** Output powers versus driving currents. **d** Emission spectra and **e** relative NIR radiant intensity during cyclic testing at a drive current of 1000 mA. **f** Relative radiant intensity during continuous operation. **h** Photograph of a 40-meter-long corridor taken with a standard camera under indoor lighting; the inset image at the bottom right shows a model photograph of the same corridor captured with an NIR camera under NIR illumination. **i** Night vision image taken 40 meters away from the NIR light source. **j-l** NIR images captured by NIR light after penetrating the back of the hand, the palm, and the wrist of a human.

Supplementary Files

This is a list of supplementary files associated with this preprint. Click to download.

- SI.docx